Quantum Computation under Micromotion in a Planar Ion Crystal

S.-T. Wang,[1,2,*] C. Shen,[1,3] and L.-M. Duan[1,2]

[1] *Department of Physics, University of Michigan, Ann Arbor, Michigan 48109, USA*
[2] *Center for Quantum Information, IIIS, Tsinghua University, Beijing 100084, PR China*
[3] *Department of Applied Physics, Yale University, New Haven, Connecticut 06511, USA*

We propose a scheme to realize scalable quantum computation in a planar ion crystal confined by a Paul trap. We show that the inevitable in-plane micromotion affects the gate design via three separate effects: renormalization of the equilibrium positions, coupling to the transverse motional modes, and amplitude modulation in the addressing beam. We demonstrate that all of these effects can be taken into account and high-fidelity gates are possible in the presence of micromotion. This proposal opens the prospect to realize large-scale fault-tolerant quantum computation within a single Paul trap.

arXiv:1408.6659v2 [quant-ph] 27 Feb 2015

Scalable quantum computation constitutes one of the ultimate goals in modern physics [1, 2]. Towards that goal, trapped atomic ions are hailed as one of the most promising platforms for the eventual realization [3, 4]. The linear Paul trap with an one-dimensional (1D) ion crystal was among the first to perform quantum logic gates [5–7] and to generate entangled states [8–10], but in terms of scalability, the 1D geometry limits the number of ions that can be successfully trapped [11, 12]. Another shortcoming of the 1D architecture is that the error threshold for fault-tolerant quantum computation with short-range gates is exceptionally low and very hard to be met experimentally [13–15].

Generic ion traps, on the other hand, could confine up to millions of ions with a 2D or 3D structure [16–18]. More crucially, large scale fault-tolerant quantum computation can be performed with a high error threshold, in the order of a percent level, with just nearest neighbor (NN) quantum gates [19–22]. This makes 2D or 3D ion crystals especially desirable for scalable quantum computation. Various 2D architectures have been proposed, including microtrap arrays [23], Penning traps [16, 24–26], and multizone trap arrays [27, 28]. However, the ion separation distance in microtraps and penning traps is typically too large for fast quantum gates since the effective ion-qubit interaction scales down rapidly with the distance. In addition, fast rotation of the ion crystal in the Penning trap makes the individual addressing of qubits very demanding. Distinct from these challenges, Paul traps provide strong confinement; however, they are hampered by the micromotion problem: fast micromotion caused by the driving radio-frequency (rf) field cannot be laser cooled. It may thus create motion of large amplitudes well beyond the Lamb-Dicke regime [29, 30], which becomes a serious impediment to high-fidelity quantum gates.

In this paper, we propose a scheme for scalable quantum computation with a 2D ion crystal in a quadrupole Paul trap. We have shown recently that micromotion may not be an obstacle for design of high-fidelity gates for the two-ion case [31]. Here, we extend this idea and show that micromotion can be explicitly taken into account in the design of quantum gates in a large ion crystal. This hence clears the critical hurdle and put Paul traps as a viable architecture to realize scalable quantum computation. In such a trap, DC and AC electrode voltages can be adjusted so that a planar ion crystal is formed with a strong trapping potential in the axial direction. In-plane micromotion is significant, but essentially no transverse micromotion is excited due to negligible displacement from the axial plane. We perform gates mediated by transverse motional modes and show that the in-plane micromotion influences the gate design through three separate ways: (1) It renormalizes the average positions of each ion compared to the static pseudopotential equilibrium positions. (2) It couples to and modifies the transverse motional modes. (3) It causes amplitude modulation in the addressing beam. In contrast to thermal motion, the fluctuation induced by micromotion is coherent and can be taken into account explicitly. Several other works also studied the effect of micromotion on equilibrium ion positions and motional modes [32–34], or used transverse modes in an oblate Paul trap to minimize the micromotion effect [35]. Here, by using multiple-segment laser pulses [36–38], we demonstrate that high-fidelity quantum gates can be achieved even in the presence of significant micromotion and even when many motional modes are excited. Our work therefore shows the feasibility of quadrupole Paul traps in performing large scale quantum computation, which may drive substantial experimental progress.

A generic quadrupole Paul trap can be formed by electrodes with a hyperbolic cross-section. The trap potential can be written as $\Phi(x, y, z) = \Phi_{\rm DC}(x, y, z) + \Phi_{\rm AC}(x, y, z)$, where

$$\Phi_{\rm DC}(x, y, z) = \frac{U_0}{d_0^2}\left[(1+\gamma)x^2 + (1-\gamma)y^2 - 2z^2\right], \quad (1)$$

$$\Phi_{\rm AC}(x, y, z) = \frac{V_0\cos(\Omega_T t)}{d_0^2}\left(x^2 + y^2 - 2z^2\right). \quad (2)$$

It contains both a DC and an AC part, with U_0 being the DC voltage, and V_0 being the AC voltage forming an electric field oscillating at the radiofrequency Ω_T. The

parameter d_0 characterizes the size of the trap and γ controls the anisotropy of the potential in the x-y plane. We choose γ to deviate slightly from zero, so that the crystal cannot rotate freely in the plane, i.e. to remove the gapless rotational mode. The AC part, on the contrary, is chosen to be isotropic in the x-y plane. We let $U_0 < 0$ such that the trapping is enhanced along the z direction in order to form a 2D crystal in the x-y plane. Disregarding the Coulomb potential first, the equations of motion of ions in such a trap can be written in the standard form of Mathieu equations along each direction:

$$\frac{d^2 r_\nu}{d\xi^2} + [a_\nu - 2q_\nu \cos(2\xi)]\, r_\nu = 0, \tag{3}$$

where $\nu \in \{x, y, z\}$, and the dimensionless parameters are $\xi = \Omega_T t/2$, $a_x = 8(1+\gamma)eU_0/md_0^2\Omega_T^2$, $a_y = 8(1-\gamma)eU_0/md_0^2\Omega_T^2$, $a_z = -16eU_0/md_0^2\Omega_T^2$, $q_x = q_y = q = -4eV_0/md_0^2\Omega_T^2$, $q_z = -2q$. Neglecting micromotion, one could approximate the potential as a time-independent harmonic pseudopotential with secular trapping frequencies $\omega_\nu = \beta_\nu \Omega_T/2$, with $\beta_\nu \approx \sqrt{a_\nu + q_\nu^2/2}$ being the characteristic exponents of the Mathieu equations [39, 40].

Results

Dynamic ion positions. Adding Coulomb interactions back, the static equilibrium positions can be found by minimizing the total pseudopotential [25, 41], or use molecular dynamics simulation with added dissipation, which imitates the cooling process in experiment [42, 43]. In our numerical simulation, we start with $N = 127$ ions forming equilateral triangles in a 2D hexagonal structure. We then solve the equations of motion with a small frictional force to find the equilibrium positions $\vec{r}^{(0)} = \vec{r}(t \to \infty) = (x_1^{(0)}, y_1^{(0)}, \cdots, x_N^{(0)}, y_N^{(0)})$, which is the starting point for the expansion of the Coulomb potential. Micromotion is subsequently incorporated by solving the decoupled driven Mathieu equations (see supplementary materials). The average ion positions $\vec{r}^{(0)}$ are found self-consistently, which differ slightly from the pseudopotential equilibrium positions (an average of $0.03\,\mu$m shift). Dynamic ion positions $\vec{r}(t)$ can be expanded successively as

$$\vec{r}(t) = \vec{r}^{(0)} + \vec{r}^{(1)} \cos(\Omega_T t) + \vec{r}^{(2)} \cos(2\Omega_T t) + \cdots . \tag{4}$$

Numerically, we found that $\vec{r}^{(1)} \approx -\frac{q}{2}\vec{r}^{(0)}$ and $\vec{r}^{(2)} \approx \frac{q^2}{32}\vec{r}^{(0)}$, where the expression for $\vec{r}^{(1)}$ is consistent with previous results [31, 32, 42]. Micromotion thus only results in breathing oscillations about the average positions.

Fig. 1(a) shows the average ion positions $\vec{r}^{(0)}$ in the planar crystal. The distribution of NN distance is plotted in figure 1(b). We choose the voltages U_0 and V_0 such that the ion distance is kept between $6.5\,\mu$m and $10\,\mu$m. This ensures that crosstalk errors due to the Gaussian

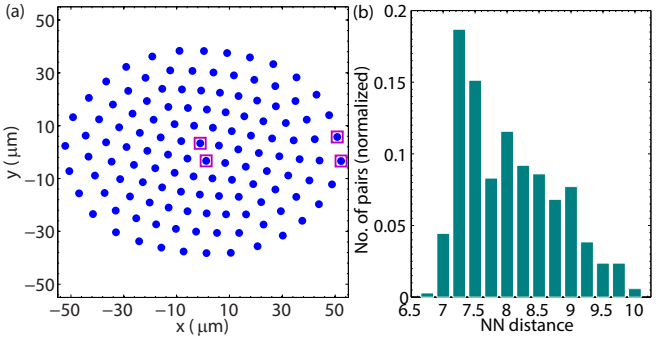

Figure 1. **Crystal structure and distance distribution.** (a) Average positions $\vec{r}^{(0)}$ of 127 ions in a planar crystal. Breathing oscillations about these average positions occur due to micromotion. Two pairs of ions (enclosed in squares), one pair in the center and one near the edge, are used for the demonstration of a quantum gate later. (b) The distribution of nearest neighbor (NN) distance. The minimum, maximum, and average NN distances are $6.9\,\mu$m, $10\,\mu$m and $8.0\,\mu$m respectively. Parameters used are: the number of ions $N = 127$; DC and AC potential $U_0 = -1.1\,$V, $V_0 = 90\,$V; AC rf frequency $\Omega_T/2\pi = 50\,$MHz; the characteristic electrode size $d_0 = 200\,\mu$m; ion mass $m = 171u$ (u is the atomic mass unit) corresponds to $^{171}\mathrm{Yb}^+$ ion; the anisotropy parameter $\gamma = 0.01$; corresponding Mathieu parameters are $a_x \approx -1.27 \times 10^{-3}, a_y \approx -1.25 \times 10^{-3}, a_z \approx 2.52 \times 10^{-3}, q \approx -0.051$, with respective secular trap frequencies $\omega_x/2\pi \approx 0.18\,$MHz, $\omega_y/2\pi \approx 0.22\,$MHz, $\omega_z/2\pi \approx 2.21\,$MHz; $\omega_z/\omega_{x,y} > 10$ ensures a planar crystal is formed.

profile of the addressing beam are negligible, at the same time maintaining strong interaction between the ions. As micromotion yields breathing oscillations, the further away the ion is from the trap center, the larger the amplitude of micromotion becomes. With the furthest ion around $52\,\mu$m from the trap center, the amplitude of micromotion is $-q/2 \times 52 \approx 1.4\,\mu$m, which is well below the separation distance between the ions but larger than the optical wavelength (see supplementary materials for the distribution of the amplitude of micromotion).

Normal modes in the transverse direction. With the knowledge of ion motion in the x-y plane, we proceed to find the normal modes and quantize the motion along the transverse (z) direction. As ions are confined in the plane, micromotion along the transverse direction is negligible. The harmonic pseudopotential approximation is therefore legitimate. Expanding the Coulomb potential to second order, we have $\frac{\partial^2}{\partial z_i \partial z_j}\left(\frac{1}{\tilde{r}_{ij}}\right)\Big|_{\vec{r}(t)} = \frac{1}{r_{ij}^3}$, where $\tilde{r}_{ij} = \sqrt{(x_i - x_j)^2 + (y_i - y_j)^2 + (z_i - z_j)^2}$ is the 3D distance and $r_{ij} = \sqrt{(x_i - x_j)^2 + (y_i - y_j)^2}$ is the planar distance between ions i and j. To the second order, transverse and in-plane normal modes are decoupled. Note that coupling between the in-plane micromotion and the transverse normal modes has been taken into account in this expansion as the Coulomb potential is expanded

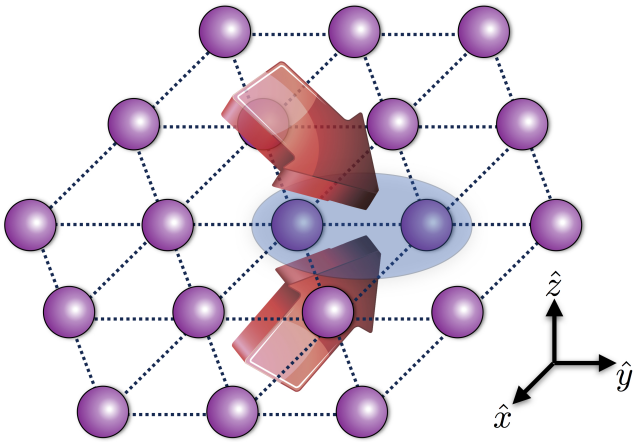

Figure 2. **Nearest neighbor quantum gate in a 2D planar crystal.** Two laser beams with a wave vector difference Δk aligned in the z direction exert a spin-dependent force on the neighboring ions. Parameters used are: The wave vector difference of addressing beams $\Delta k = 8\,\mu\mathrm{m}^{-1}$; Laser beams are assumed to take a Gaussian profile with a beam waist $w = 3\,\mu$m centered at the average positions of the respective ion; The Lamb-Dicke parameter $\eta_z = \Delta k\sqrt{\hbar/2m\omega_z} \approx 0.029$. Other parameters are the same as in Fig. 1.

around the dynamic ion positions $\vec{r}(t)$. With significant in-plane micromotion, distances between ions are time-dependent, which in turn affects the transverse modes. We can expand the quadratic coefficients in series:

$$\frac{1}{r_{ij}^3} \approx \left\langle \frac{1}{r_{ij}^3} \right\rangle + M_{ij}\cos(\Omega_T t) + \cdots . \tag{5}$$

The time-averaged coefficients $\langle 1/r_{ij}^3 \rangle$ can be used to compute the transverse normal modes. The next order containing $\cos(\Omega_T t)$ terms can be considered as a time-dependent perturbation to the Hamiltonian. It contributes on the order of $O\left(q\omega_k^2/\Omega_T^2\right) \sim O(qq_z^2)$ in the rotating wave approximation, where ω_k is the transverse mode frequency. The term $\langle 1/r_{ij}^3 \rangle \approx \left(1/r_{ij}^{(0)}\right)^3(1 - 3q^2/4) + O(q^3)$, where $r_{ij}^{(0)}$ is the ion distance computed with $\vec{r}^{\,(0)}$ without considering micromotion (see supplementary materials). Here, the micromotion effect is an overall renormalization in the term $1/r_{ij}^3$, so it does not modify the normal mode structure. Instead, it slightly shifts down the transverse mode frequencies (in the order of $O(q^2)$). Numerically, we found an average reduction of around 0.4 kHz in each transverse mode frequency with our chosen parameters. Although mode structure is not altered by this overall renormalization, the discrepancy in equilibrium positions compared to the pseudopotential approximation will modify both the normal mode structure and mode frequencies.

High-fidelity quantum gates. After obtaining the correct transverse normal modes, we now show how to design high-fidelity quantum gates with in-plane micromotion. Since NN gates are sufficient for fault-tolerant quantum computation in a planar crystal, we show as a demonstration that high-fidelity entangling gates can be achieved with a pair of NN ions in the trap center and near the trap edge. One may perform the gate along the transverse direction by shining two laser beams on the two NN ions with wave vector difference $\Delta k\hat{z}$ and frequency difference μ (see Fig. 2) [38, 44]. The laser-ion interaction Hamiltonian is [37] $H = \sum_{j=1}^{2} \hbar\Omega_j \cos(\Delta k \cdot \delta z_j + \mu t)\sigma_j^z$, where Ω_j is the (real) Raman Rabi frequency for the jth ion, σ_j^z is the Pauli-Z matrix acting on the pseudospin space of internal atomic states of the ion j, and δz_j is the ion displacement from the equilibrium position. Quantize the ion motion, $\delta z_j = \sum_k \sqrt{\hbar/2m\omega_k} b_j^k (a_k + a_k^\dagger)$, with b_j^k (ω_k) being the mode vector (frequency) for mode k and $a_k^\dagger$ creates the k-th phonon mode. Expanding the cosine term and ignoring the single-bit operation, the Hamiltonian can be written in the interaction picture as

$$H_{\mathrm{I}} = -\sum_{j=1}^{2}\sum_{k} \chi_j(t) g_j^k \left(a_k^\dagger e^{i\omega_k t} + a_k e^{-i\omega_k t}\right)\sigma_j^z, \tag{6}$$

where $\chi_j(t) = \hbar\Omega_j \sin(\mu t)$, $g_j^k = \eta_k b_j^k$, and the Lamb-Dicke parameter $\eta_k = \Delta k\sqrt{\hbar/2m\omega_k} \ll 1$. The evolution operator corresponding to the Hamiltonian H_{I} can be written as [37, 38, 45]

$$U(\tau) = \exp\left(i\sum_j \phi_j(\tau)\sigma_j^z + i\sum_{j<n}\phi_{jn}(\tau)\sigma_j^z\sigma_n^z\right), \tag{7}$$

where the qubit-motion coupling term $\phi_j(\tau) = -i\sum_k \alpha_j^k(\tau)a_k^\dagger - \alpha_j^{k*}(\tau)a_k$ with $\alpha_j^k(\tau) = \frac{i}{\hbar}g_j^k\int_0^\tau \chi_j(t)e^{i\omega_k t}dt$ and the two-qubit conditional phase $\phi_{jn}(\tau) = \frac{2}{\hbar^2}\sum_k g_j^k g_n^k \int_0^\tau\int_0^{t_2} \chi_j(t_2)\times\chi_n(t_1)\sin(\omega_k(t_2 - t_1))dt_1dt_2$. To realize a conditional phase flip (CPF) gate between ions j and n, we require $\alpha_j^k \approx 0$ so that the spin and phonons are almost disentangled at the end of the gate, and also $\phi_{jn}(\tau) = \pi/4$. It is worthwhile to note that in deriving Eq. (7), we dropped single-qubit operations as we are interested in the CPF gate. These fixed single-qubit operations can be explicitly compensated in experiment by subsequent rotations of single spins. (see supplementary materials for more detailed derivation and analysis).

As the number of ions increases, transverse phonon modes become very close to each other in frequencies. During typical gate time, many motional modes will be excited. We use multiple-segment pulses to achieve a high-fidelity gate [36, 37]. The total gate time is divided into m equal-time segments, and the Rabi frequency takes the form $\Omega_j(t) = \Omega_j^{(i)}\Omega_j^{\mathrm{G}}(t)$, with $\Omega_j^{(i)}$ being the controllable and constant amplitude for the ith segment ($(i-1)\tau/m \le t < i\tau/m$). Due to the in-plane micromotion, the laser profile $\Omega_j^{\mathrm{G}}(t)$ seen by the

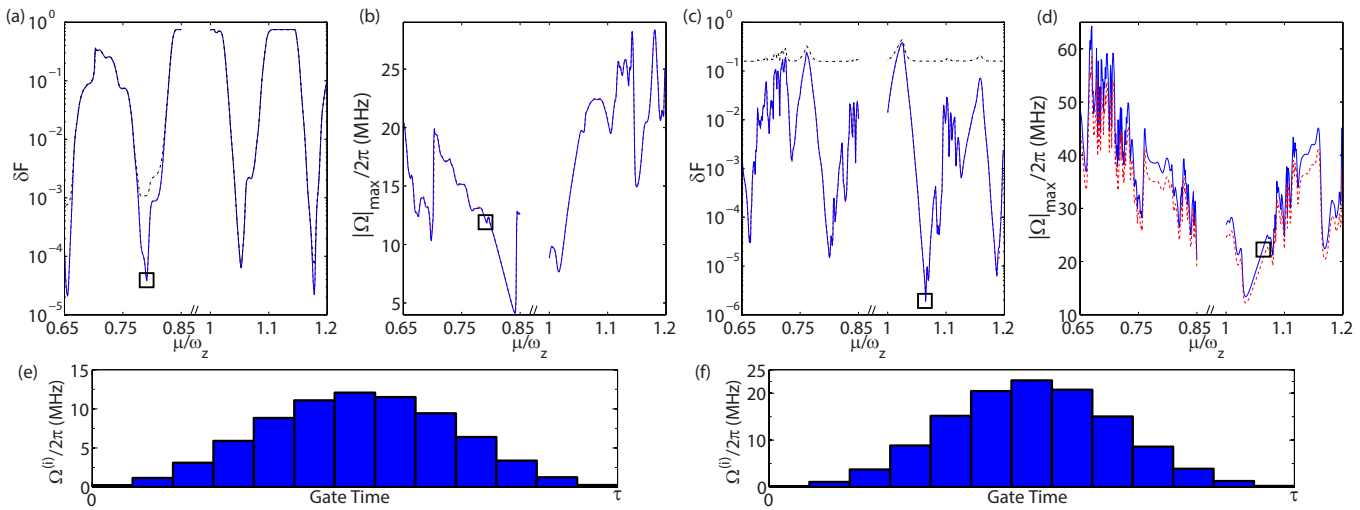

Figure 3. **Gate infidelity and pulse shaping.** (a), (b), and (e) are respectively the gate infidelity, the maximum Rabi frequency, and the thirteen-segment pulse pattern corresponding to the results marked by squares, for the center pair as labeled in Fig. 1. (c), (d), and (f) are the corresponding plots for the edge pair. The blue solid lines and the pulse sequences indicate the optimal results with micromotion considered. The red dashed lines are results for a genuine static harmonic trap without micromotion. Black dash-dot lines in (a) and (c) are obtained by applying the optimal solution for a static trap to the case with micromotion. All transverse modes are distributed between $0.85\omega_z$ and ω_z. We optimize the gate near either end of the spectrum. The optimal results marked by the squares are $\delta F = 4\times10^{-5}$ and $|\Omega|_{\max}/2\pi = 12\,\mathrm{MHz}$ ($\delta F = 4\times10^{-6}$ and $|\Omega|_{\max}/2\pi = 22\,\mathrm{MHz}$) for the center (edge) pair. Parameters used are: total gate time $\tau = 50\times 2\pi/\omega_z \approx 23\,\mu\mathrm{s}$; $m = 13$ segments are used; Doppler temperature $k_BT_D/\hbar \approx 2\pi\times 10\,\mathrm{MHz}$ is assumed for all phonon modes. Other parameters are the same as in Fig. 1 and Fig. 2.

ion is time-dependent. In our calculation, we assume the Raman beam to take a Gaussian form, with $\Omega_j^{\mathrm{G}}(t) = \exp\left\{-\left[\left(x_j(t)-x_j^{(0)}\right)^2+\left(y_j(t)-y_j^{(0)}\right)^2\right]/w^2\right\}$, where w is the beam waist and $\left(x_j^{(0)},y_j^{(0)}\right)$ are the average positions for the jth ion. Any other beam profile can be similarly incorporated.

To gauge the quality of the gate, we use a typical initial state for the ion spin $|\Phi_0\rangle = (|0\rangle+|1\rangle)\otimes(|0\rangle+|1\rangle)/2$ and the thermal state ρ_m for the phonon modes at the Doppler temperature. The fidelity is defined as $F = \mathrm{tr}_m\left[\rho_m\left|\langle\Psi_0|U_{\mathrm{CPF}}^{\dagger}U(\tau)|\Psi_0\rangle\right|^2\right]$ tracing over the phonon modes, with the evolution operator $U(\tau)$ and the perfect CPF gate $U_{\mathrm{CPF}} \equiv e^{i\pi\sigma_1^z\sigma_2^z}$. For simplicity, we take $\Omega_j^{(i)} = \Omega_n^{(i)} = \Omega^{(i)}$ for the ions j and n. For any given detuning μ and gate time τ, we optimize the control parameters $\Omega^{(i)}$ to get the maximum fidelity F. Fig. 3 shows the gate infidelity $\delta F = 1-F$ and the maximum Rabi frequency $|\Omega|_{\max} = \max_i \Omega^{(i)}$ for the center pair [(a) and (b)] and the edge pair [(c) and (d)] with 13 segments and a relatively fast gate $\tau \approx 23\,\mu\mathrm{s}$. Detuning μ can be used as an adjusting parameter in experiment to find the optimal results. All transverse phonon modes are distributed between $0.85\omega_z$ and ω_z. We optimize the gate near either end of the spectrum since optimal results typically occur there. Blue solid lines indicate the optimal results with micromotion and red dashed lines show the results for a genuine static harmonic trap, which are almost identical in (a), (b) and (c). It implies that micromotion can almost be completely compensated, but with a stronger laser power for the edge pair. If we apply the optimal result for the static trap to the realistic case with micromotion, the fidelity will be lower as indicated by the black dash-dot lines. This is especially so for the edge pair, where the fidelity is lower than 85% at any detuning. It is therefore critical to properly include the effect of micromotion. With corrected pulse sequences, a fidelity $F > 99.99\%$ can be attained with $|\Omega|_{\max}/2\pi \approx 12\,\mathrm{MHz}$ ($|\Omega|_{\max}/2\pi \approx 22\,\mathrm{MHz}$) for the center (edge) ions. The Rabi frequencies can be further reduced by a slower gate and/or more pulse segments.

Noise estimation. Micromotion of any amplitude does not induce errors to the gates as it has been completely compensated in our gate design. We now estimate various other sources of noise for gate implementation. In considering the effect of in-plane micromotion to the transverse modes, we are accurate to the order of q^2, so an error of $q^3 \approx 10^{-4}$ is incurred. The actual error is smaller since the Coulomb potential is an order of magnitude smaller than the trapping potential along the transverse direction. The cross-talk error probability due to beam spillover is $P_c = e^{-2(d/w)^2} < 2\times10^{-5}$, with the ion distance $d \gtrsim 7\,\mu\mathrm{m}$ and the beam waist $w = 3\,\mu\mathrm{m}$. At the Doppler temperature $k_BT_D/\hbar \approx 2\pi\times 10\,\mathrm{MHz}$,

thermal spread in positions may degrade the gate fidelity. Similar to micromotion, thermal motion causes the effective Rabi frequency to fluctuate. With $\omega_{x,y}/2\pi \approx 0.2\,\mathrm{MHz}$, there is a mean phonon number $\bar{n}_0 \approx 50$ in the x-y plane. It gives rise to thermal motion with average fluctuation in positions, $\delta r \approx 0.23\,\mu\mathrm{m}$, which can be estimated as in Ref. 46. The resultant gate infidelity is $\delta F_1 \approx (\pi^2/4)(\delta r/w)^4 \approx 10^{-4}$. Lastly, we estimate the infidelity caused by higher-order expansion in the Lamb-Dicke parameter. The infidelity is $\delta F_2 \approx \pi^2\eta_z^4(\bar{n}_z^2 + \bar{n}_z + 1/8) \approx 2\times 10^{-4}$, where $\bar{n}_z \approx 5$ is the mean phonon number in the transverse direction [37]. Other than the effects considered above, micromotion may also lead to rf heating when it is coupled to thermal motion. However, simulation has shown that at low temperature $T < 10\,\mathrm{mK}$ and small q parameters, rf heating is negligible [42, 47]. Heating effect due to rf phase shift and voltage fluctuation should also be negligible when they are well-controlled [42].

Discussion

It is worthwhile to point out that although we have demonstrated the feasibility of our gate design via a single case with $N = 127$ ions, the proposed scheme scales for larger crystals. The intuition is that through optimization of the segmented pulses, all phonon modes are nearly disentangled from the quantum qubits at the end of the gate. However, as the number of ions further increases, one would presumably need more and more precise control for all the experimental parameters ($< 1\%$ fluctuation in voltage for example). rf heating may also destabilize a much larger crystal [48], and more careful studies are necessary for larger crystals.

One may also notice that in Ref. 31, we considered gates mediated by the longitudinal phonon modes, so the effect of micromotion is a phase modulation. Here, we utilize transverse modes so the amplitude of the laser beam is modulated. There are a few advantages in using the transverse modes: first, it is experimentally easier to access the transverse phonon modes in a planar ion crystal; second, in a planar crystal, the transverse direction is tightly trapped, so micromotion along that direction can be neglected; third, the transverse phonon modes do not couple to the in-plane modes and the in-plane micromotion affects the transverse modes via the time-dependence of the equilibrium positions, the effect of which is again suppressed due to tight trapping in the transverse direction.

In summary, we have demonstrated that a planar ion crystal in a quadrupole Paul trap is a promising platform to realize scalable quantum computation when micromotion is taken into account explicitly. We show that the in-plane micromotion comes into play through three separate effects, and each of them can be resolved. This paves a new pathway for large-scale trapped-ion quantum computation.

* Correspondence and requests for materials should be addressed to S.-T.W. (wangst@umich.edu)

[1] Nielsen, M. A. & Chuang, I. L. *Quantum computation and quantum information* (Cambridge university press, 2010).

[2] Ladd, T. D. *et al.* Quantum computers. *Nature* **464**, 45–53 (2010).

[3] Blatt, R. & Wineland, D. Entangled states of trapped atomic ions. *Nature* **453**, 1008–1015 (2008).

[4] Haffner, H., Roos, C. F. & Blatt, R. Quantum computing with trapped ions. *Phys. Rep.* **469**, 155–203 (2008).

[5] Cirac, J. I. & Zoller, P. Quantum computations with cold trapped ions. *Phys. Rev. Lett.* **74**, 4091–4094 (1995).

[6] Monroe, C., Meekhof, D. M., King, B. E., Itano, W. M. & Wineland, D. J. Demonstration of a fundamental quantum logic gate. *Phys. Rev. Lett.* **75**, 4714–4717 (1995).

[7] Schmidt-Kaler, F. *et al.* Realization of the cirac-zoller controlled-not quantum gate. *Nature* **422**, 408–411 (2003).

[8] Turchette, Q. A. *et al.* Deterministic entanglement of two trapped ions. *Phys. Rev. Lett.* **81**, 3631–3634 (1998).

[9] Sackett, C. A. *et al.* Experimental entanglement of four particles. *Nature* **404**, 256–259 (2000).

[10] Roos, C. F. *et al.* Control and measurement of three-qubit entangled states. *Science* **304**, 1478–1480 (2004).

[11] Raizen, M. G., Gilligan, J. M., Bergquist, J. C., Itano, W. M. & Wineland, D. J. Ionic crystals in a linear paul trap. *Phys. Rev. A* **45**, 6493–6501 (1992).

[12] Schiffer, J. P. Phase transitions in anisotropically confined ionic crystals. *Phys. Rev. Lett.* **70**, 818–821 (1993).

[13] Gottesman, D. Fault-tolerant quantum computation with local gates. *J. Mod. Opt.* **47**, 333–345 (2000).

[14] Svore, K. M., Terhal, B. M. & DiVincenzo, D. P. Local fault-tolerant quantum computation. *Phys. Rev. A* **72**, 022317 (2005).

[15] Szkopek, T. *et al.* Threshold error penalty for fault-tolerant quantum computation with nearest neighbor communication. *IEEE Trans. Nanotechnol.* **5**, 42–49 (2006).

[16] Itano, W. M. *et al.* Bragg diffraction from crystallized ion plasmas. *Science* **279**, 686–689 (1998).

[17] Drewsen, M., Brodersen, C., Hornekær, L., Hangst, J. & Schifffer, J. Large ion crystals in a linear paul trap. *Phys. Rev. Lett.* **81**, 2878–2881 (1998).

[18] Mortensen, A., Nielsen, E., Matthey, T. & Drewsen, M. Observation of three-dimensional long-range order in small ion coulomb crystals in an rf trap. *Phys. Rev. Lett.* **96**, 103001 (2006).

[19] Raussendorf, R. & Harrington, J. Fault-tolerant quantum computation with high threshold in two dimensions. *Phys. Rev. Lett.* **98**, 190504 (2007).

[20] Raussendorf, R., Harrington, J. & Goyal, K. Topological fault-tolerance in cluster state quantum computation. *New J. Phys.* **9**, 199 (2007).

[21] Fowler, A. G., Stephens, A. M. & Groszkowski, P. High-threshold universal quantum computation on the surface code. *Phys. Rev. A* **80**, 052312 (2009).

[22] DiVincenzo, D. P. Fault-tolerant architectures for superconducting qubits. *Physica Scripta* **2009**, 014020 (2009).

[23] Cirac, J. I. & Zoller, P. A scalable quantum computer with ions in an array of microtraps. *Nature* **404**, 579–581

(2000).
[24] Porras, D. & Cirac, J. I. Quantum manipulation of trapped ions in two dimensional coulomb crystals. *Phys. Rev. Lett.* **96**, 250501 (2006).
[25] Zou, P., Xu, J., Song, W. & Zhu, S.-L. Implementation of local and high-fidelity quantum conditional phase gates in a scalable two-dimensional ion trap. *Phys. Lett. A* **374**, 1425–1430 (2010).
[26] Mitchell, T. B. *et al.* Direct observations of structural phase transitions in planar crystallized ion plasmas. *Science* **282**, 1290–1293 (1998).
[27] Kielpinski, D., Monroe, C. & Wineland, D. J. Architecture for a large-scale ion-trap quantum computer. *Nature* **417**, 709–711 (2002).
[28] Monroe, C. & Kim, J. Scaling the ion trap quantum processor. *Science* **339**, 1164–1169 (2013).
[29] Berkeland, D., Miller, J., Bergquist, J., Itano, W. & Wineland, D. Minimization of ion micromotion in a paul trap. *J. Appl. Phys.* **83**, 5025–5033 (1998).
[30] Leibfried, D., Blatt, R., Monroe, C. & Wineland, D. Quantum dynamics of single trapped ions. *Rev. Mod. Phys.* **75**, 281–324 (2003).
[31] Shen, C. & Duan, L.-M. High-fidelity quantum gates for trapped ions under micromotion. *Phys. Rev. A* **90**, 022332 (2014).
[32] Landa, H., Drewsen, M., Reznik, B. & Retzker, A. Modes of oscillation in radiofrequency paul traps. *New J. Phys.* **14**, 093023 (2012).
[33] Kaufmann, H. *et al.* Precise experimental investigation of eigenmodes in a planar ion crystal. *Phys. Rev. Lett.* **109**, 263003 (2012).
[34] Landa, H., Retzker, A., Schaetz, T. & Reznik, B. Entanglement generation using discrete solitons in coulomb crystals. *Phys. Rev. Lett.* **113**, 053001 (2014).
[35] Yoshimura, B., Stork, M., Dadic, D., Campbell, W. C. & Freericks, J. K. Creation of two-dimensional coulomb crystals of ions in oblate Paul traps for quantum simulations. *ArXiv e-prints* (2014). 1406.5545.
[36] Zhu, S.-L., Monroe, C. & Duan, L.-M. Arbitrary-speed quantum gates within large ion crystals through minimum control of laser beams. *Europhys. Lett.* **73**, 485 (2006).
[37] Zhu, S.-L., Monroe, C. & Duan, L.-M. Trapped ion quantum computation with transverse phonon modes. *Phys. Rev. Lett.* **97**, 050505 (2006).
[38] Choi, T. *et al.* Optimal quantum control of multimode couplings between trapped ion qubits for scalable entanglement. *Phys. Rev. Lett.* **112**, 190502 (2014).
[39] McLachlan, N. W. *Theory and application of Mathieu functions* (Clarendon Press, 1951).
[40] King, B. E. *Quantum state engineering and information processing with trapped ions.* Ph.D. thesis, University of Colorado (1999).
[41] James, D. Quantum dynamics of cold trapped ions with application to quantum computation. *Appl. Phys. B* **66**, 181–190 (1998).
[42] Zhang, C. B., Offenberg, D., Roth, B., Wilson, M. A. & Schiller, S. Molecular-dynamics simulations of cold single-species and multispecies ion ensembles in a linear paul trap. *Phys. Rev. A* **76**, 012719 (2007).
[43] Schiffer, J. P., Drewsen, M., Hangst, J. S. & Hornekær, L. Temperature, ordering, and equilibrium with time-dependent confining forces. *Proc. Natl. Acad. Sci.* **97**, 10697–10700 (2000).
[44] Leibfried, D. *et al.* Experimental demonstration of a robust, high-fidelity geometric two ion-qubit phase gate. *Nature* **422**, 412–415 (2003).
[45] Kim, K. *et al.* Entanglement and tunable spin-spin couplings between trapped ions using multiple transverse modes. *Phys. Rev. Lett.* **103**, 120502 (2009).
[46] Lin, G.-D. *et al.* Large-scale quantum computation in an anharmonic linear ion trap. *Europhys. Lett.* **86**, 60004 (2009).
[47] Ryjkov, V. L., Zhao, X. & Schuessler, H. A. Simulations of the rf heating rates in a linear quadrupole ion trap. *Phys. Rev. A* **71**, 033414 (2005).
[48] Buluta, I., Kitaoka, M., Georgescu, S. & Hasegawa, S. Investigation of planar coulomb crystals for quantum simulation and computation. *Phys. Rev. A* **77**, 062320 (2008).

Acknowledgments

We would like to thank T. Choi and Z.-X. Gong for useful discussions. This work was supported by the NBRPC (973 Program) No. 2011CBA00300 (No. 2011CBA00302), the IARPA MUSIQC program, the ARO, and the AFOSR MURI program.

Author contributions

C.S. and L.-M.D. conceived the idea. S.-T.W. and C.S. carried out the calculations. S.-T.W. and L.-M.D. wrote the manuscript. All authors contributed to the discussion of the project and revision of the manuscript.

Additional information

Supplementary information is available.

Competing financial interests: The authors declare no competing financial interests.

SUPPLEMENTARY INFORMATION: QUANTUM COMPUTATION UNDER MICROMOTION IN A PLANAR ION CRYSTAL

In this supplementary information, we provide more details on the iterative method to find dynamic ion positions, and also consider the effect of in-plane micromotion to the transverse normal modes. We also include a more detailed derivation for the Hamiltonian and time-evolution operator for a two-ion entangling gate.

ITERATIVE METHOD TO FIND DYNAMIC ION POSITIONS

As discussed in the main text, the equations of motion in each direction can be written in the standard form of Mathieu equations (neglecting Coulomb potential):

$$\frac{d^2 r_\nu}{d\xi^2} + [a_\nu - 2q_\nu \cos(2\xi)]\, r_\nu = 0, \tag{8}$$

where $\nu \in \{x, y, z\}$, $\xi = \Omega_T t/2$, and dimensionless parameters a_ν and q_ν are defined in the main text. The characteristic exponents β_ν can be computed from a_ν and q_ν iteratively [39]. A pseudopotential can then be obtained with secular frequencies $\omega_\nu = \beta_\nu \Omega_T/2$ and

$$e\,(\Phi_{\rm DC} + \Phi_{\rm AC}) \approx \frac{1}{2} m\omega_x^2 x^2 + \frac{1}{2} m\omega_y^2 y^2 + \frac{1}{2} m\omega_z^2 z^2. \tag{9}$$

Assuming tight trapping along the z direction, i.e. $\omega_z/\omega_{x,y} > 10$, a planar crystal is formed in the x-y plane. Adding the Coulomb potential V_C, one acquires a time-independent potential in the plane:

$$V_{\rm pseudo}(x,\, y) = \sum_i \left(\frac{1}{2} m\omega_x^2 x_i^2 + \frac{1}{2} m\omega_y^2 y_i^2 \right) + \sum_{i<j} \frac{e^2}{4\pi\epsilon_0 \sqrt{(x_i - x_j)^2 + (y_i - y_j)^2}}. \tag{10}$$

$i = 1, 2, \cdots, N$, where N is the number of ions. Numerically, we start with $N = 127$ ions forming equilateral triangles in a 2D hexagonal structure [Fig. 4(a)], and find the static equilibrium positions $\vec{r}^{\,(0)} = (x_1^{(0)}, y_1^{(0)}, \cdots, x_N^{(0)}, y_N^{(0)})$ under this pseudopotential approximation by solving the classical equations of motion with a frictional force $(-\eta(\dot{x} + \dot{y}))$, simulating the cooling process in experiment. This set of static equilibrium positions [marked by squares in Fig. 4(b)] is the starting point to derive the oscillatory behavior of each ion under micromotion.

In a planar crystal, the ions oscillate slightly around their average positions, so it is appropriate to expand the Coulomb potential around the equilibrium positions $\vec{r}^{\,(0)}$. To the second order, the Coulomb potential can be written in a quadratic form:

$$V_C \approx \frac{1}{2} \vec{r}^{\,T} M_C \vec{r} + \vec{g}^{\,T} \vec{r} + \text{constant term}, \tag{11}$$

where $\vec{r} = (x_1, y_1, \cdots, x_N, y_N)$, M_C is a $2N \times 2N$ matrix, and $\vec{g}$ is a $2N$-vector. The trapping potential can also be written in this coordinate basis:

$$e\,(\Phi_{\rm DC} + \Phi_{\rm AC}) = \frac{1}{2} \vec{r}^{\,T} M_{DC} \vec{r} + \frac{V_0}{d_0^2} \cos(\Omega_T t) \vec{r}^{\,T} I_{2N}\, \vec{r}, \tag{12}$$

where I_{2N} is the $2N \times 2N$ identity matrix, and M_{DC} is a diagonal matrix with $2(1+\gamma)eU_0/d_0^2$ in the odd rows (x coordinates), and $2(1-\gamma)eU_0/d_0^2$ in the even rows (y coordinates). Therefore, the total potential energy is

$$V = \frac{1}{2} \vec{r}^{\,T} (M_{DC} + M_C) \vec{r} + \frac{V_0}{d_0^2} \cos(\Omega_T t) \vec{r}^{\,T} I_{2N}\, \vec{r} + \vec{g}^{\,T} \vec{r}. \tag{13}$$

Note that the time-dependent part of the potential is isotropic in the coordinates, so it does not couple each Mathieu equations. We can find an orthogonal matrix Q that diagonalizes the first term, i.e. $Q(M_{DC} + M_C)Q^T = \Lambda$. Using the normal coordinates $\vec{s} = Q\vec{r}$, the equations of motion form decoupled Mathieu equations:

$$\frac{d^2 s_i}{d\xi^2} + (a_i - 2q_i \cos(2\xi)) s_i = f_i, \tag{14}$$

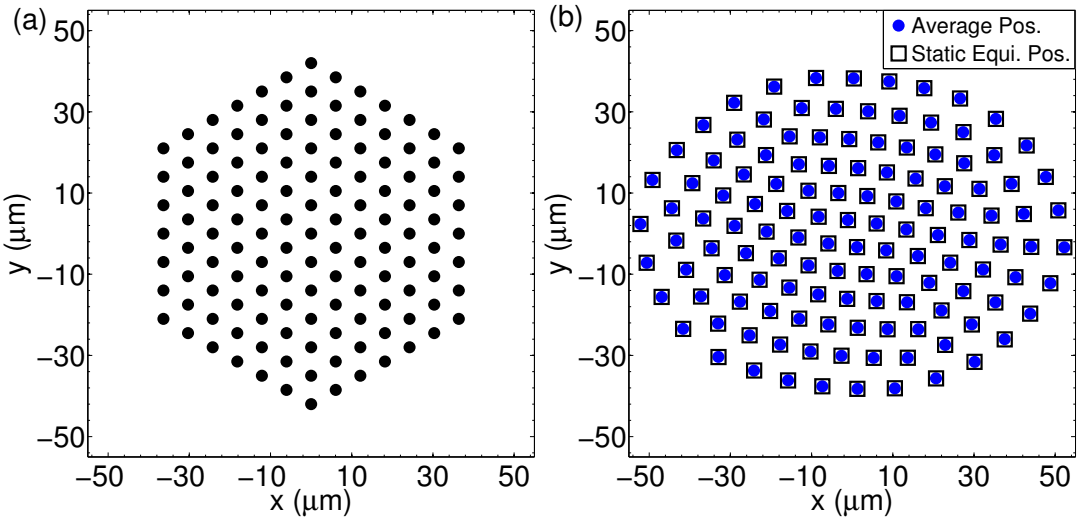

Figure 4. (a) Initial configuration for ion crystal. 127 ions forming equilateral triangles with ion distance 7 μm are arranged in a 2D hexagonal structure. (b) Stable ion configuration under the trap and Coulomb potential. Static equilibrium positions under the pseudopotential approximation are marked by (black) squares. Average ion positions found self-consistently by solving the Mathieu equations are marked by (blue) dots. The difference between two sets of equilibrium positions is around 0.03 μm on average, which is hardly visible in the figure.

where $a_i = 4\Lambda_{ii}/m\Omega_T^2$, $q_i = q = -4eV_0/md_0^2\Omega_T^2$, and $f_i = -\frac{4}{m\Omega_T^2}(Q\vec{g})_i$. The inhomogeneous Mathieu equations can be solved by substituting a special solution in the form of $s_i = f_i\sum_{n=0}^{\infty} c_i^{(n)}\cos(2n\xi)$, and the series coefficients $c_i^{(n)}$ can be computed numerically [31]. After that, the ion coordinates can be transformed back to the Cartesian coordinates $\vec{r} = Q^T\vec{s}$, where $\vec{r}$ can be expressed successively as

$$\vec{r} = \vec{r}^{(0)} + \vec{r}^{(1)}\cos(2\xi) + \vec{r}^{(2)}\cos(4\xi) + \cdots . \tag{15}$$

$\vec{r}^{(0)}$ now becomes the new average (equilibrium) positions, and can be substituted back to the expansion in equation (11). The ion positions $\vec{r}$ can be attained self-consistently in this manner. A dynamical expansion of the Coulomb potential around $\vec{r}^{(0)} + \vec{r}^{(1)}\cos(2\xi)$ may yield a more accurate result for the normal modes in the plane [32]. For our purpose, the static expansion is sufficient as we only need accurate ion positions $\vec{r}$ to compute the normal modes along the z direction. Numerically, we found that $\vec{r}^{(1)} \approx -\frac{q}{2}\vec{r}^{(0)}$ and $\vec{r}^{(2)} \approx \frac{q^2}{32}\vec{r}^{(0)}$, which are consistent with previous results [31, 32]. Hence, micromotion only results in breathing oscillations about the average positions of each ion. The further the ion is from the center of the trap, the larger the amplitude of micromotion becomes.

Fig. 5 shows the amplitude of micromotion for each ion. The largest amplitude for the edge ion is around 1.35 μm, which is well below the ion separation ($7 \sim 10\,\mu$m), necessary for the formation of a well-defined crystal and for individual addressing.

NORMAL MODES ALONG THE TRANSVERSE DIRECTION

With the knowledge of the motion of ions in the x-y plane, we could find the normal modes and quantize the motion along the transverse (z) direction. As ions are confined in the plane, micromotion along the transverse direction is negligible. A harmonic pseudopotential is thus valid for the z direction. Expanding the Coulomb potential to second order again, we have

$$V_z = \frac{1}{2}m\omega_z^2\sum_i z_i^2 + \frac{e^2}{4\pi\epsilon_0}\left[\sum_{i\neq j}\left(\frac{1}{r_{ij}^3}\right)z_i z_j - \sum_{i\neq j}\left(\frac{1}{r_{ij}^3}\right)z_i^2\right], \tag{16}$$

where $r_{ij} = \sqrt{(x_i - x_j)^2 + (y_i - y_j)^2}$. $x_i(t)$ and $y_i(t)$ are time-dependent though, due to the in-plane micromotion. From here, we can see explicitly that the transverse modes are decoupled from the planar modes. Expanding the term

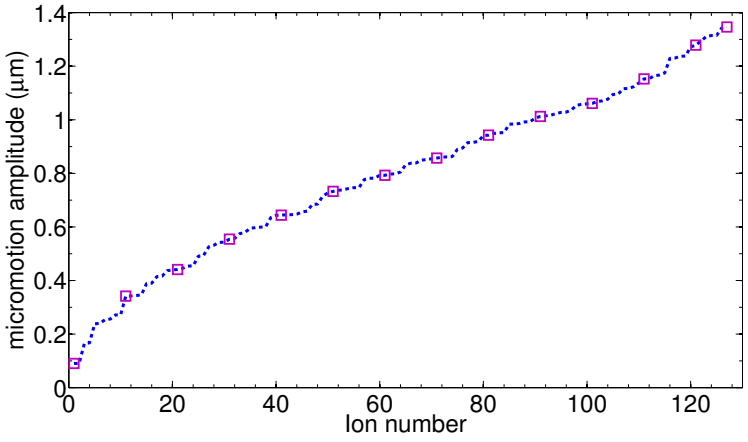

Figure 5. Amplitude of micromotion for each ion (sorted in increasing order).

$1/r_{ij}^3(t)$ in series, one has

$$\frac{1}{r_{ij}^3} \approx \left\langle \frac{1}{r_{ij}^3} \right\rangle + M_{ij}\cos(\Omega_T t) + \cdots \tag{17}$$

The matrix element M_{ij} is in the order of $O(q)$ and can be obtained numerically from $\langle \cos(\Omega_T t)/r_{ij}^3 \rangle$. To have an intuitive understanding of the effect of micromotion on transverse modes, we take positions $\vec{r}$ in the form of Eq. (15), obtaining

$$\frac{1}{r_{ij}^3} \approx \left(\frac{1}{r_{ij}^{(0)}}\right)^3 \left(1 - \frac{q}{2}\cos(\Omega_T t) + \frac{q^2}{32}\cos(2\Omega_T t)\right)^{-3} + O(q^3), \tag{18}$$

where $r_{ij}^{(0)}$ is the zeroth order approximation using the average positions $\vec{r}^{\,(0)}$ without considering micromotion. Thus, $\langle 1/r_{ij}^3 \rangle \approx \left(1/r_{ij}^{(0)}\right)^3 (1 - 3q^2/4) + O(q^3)$, where we used the fact that $\langle \cos(\Omega_T t) \rangle = 0$ and $\langle \cos^2(\Omega_T t) \rangle = 1/2$. From the time-independent term $\langle 1/r_{ij}^3 \rangle$, we diagonalize V_z and find the normal modes as well as the eigenenergies in the transverse direction. Subsequently, we quantize the total Hamiltonian (with kinetic energy) and write $H = \sum_k \hbar\omega_k a_k^\dagger a_k$, where a_k is the annihilation operator for the quantized phonon mode, and ω_k is the corresponding eigenfrequency. In the interaction picture, $a_k \to a_k e^{-i\omega_k t}$. The time-dependent term containing $\cos(\Omega_T t)$ can then be treated as a perturbation; under the rotating wave approximation, since $\Omega_T \gg \omega_k$, the term affects the normal modes to the order of $O\left(q\omega_k^2/\Omega_T^2\right) \sim O(qq_z^2)$, which can be safely neglected. Since the first term in V_z is diagonal in z_i and the second term is reduced by a factor $(1 - 3q^2/4)$ by micromotion, the normal mode structure remains unchanged, and the mode frequencies are reduced slightly.

TWO-ION ENTANGLING GATE

The spin-dependent force on an ion is due to the AC Stark shift on each spin state. A different shift on the two internal spin states of an ion results in a Hamiltonian

$$H = \hbar \frac{|\Omega_{\rm eg}|^2}{4\delta} \sigma^z, \tag{19}$$

where $\Omega_{\rm eg}$ is the Rabi frequency of the laser beam and δ is the detuning from the excited state. By shining two laser beams at an angle with wave vectors $\mathbf{k}_1$, $\mathbf{k}_2$ and frequencies ω_1, ω_2, we have

$$\Omega_{\rm eg} = \Omega_0 \left(e^{i(\mathbf{k}_1 \cdot \mathbf{r} + \omega_1 t + \phi)} + e^{i(\mathbf{k}_2 \cdot \mathbf{r} + \omega_2 t)} \right), \tag{20}$$

where ϕ is the phase difference between two beams. So we have

$$H = \hbar\Omega \left(1 + \cos(\Delta k \cdot z + \mu t + \phi)\right) \sigma^z, \tag{21}$$

where $\Omega = \Omega_0^2/2\delta$ is the effective two-photon Rabi frequency, $\Delta k\hat{z} = \mathbf{k}_1 - \mathbf{k}_2$ is aligned along the z direction, and $\mu = \omega_1 - \omega_2$. As we are mostly interested in the two-qubit entangling gate, which is the building block for universal quantum gates, we consider laser beams shining on two ions, and ignore the first term $\hbar\Omega\sigma^z$ in the Hamiltonian that only induces single bit operations. We therefore have

$$H = \sum_{j=1}^{2} \hbar\Omega_j \cos(\Delta k \cdot z_j + \mu t + \phi_j)\sigma_j^z, \tag{22}$$

The ion position $z_j = z_{j0} + \delta z_j$, where z_{j0} is the equilibrium position and δz_j is the small displacement. We dump the term $\Delta k \cdot z_{j0}$ to the phase ϕ_j, and expand the cosine term in the Lamb-Dicke limit $\Delta k \cdot \delta z_j \ll 1$,

$$H = \sum_{j=1}^{2} \hbar\Omega_j \cos(\Delta k \cdot \delta z_j + \mu t + \phi_j)\sigma_j^z \tag{23}$$

$$\approx -\sum_{j=1}^{2} \hbar\Omega_j \sin(\Delta k \cdot \delta z_j) \sin(\mu t + \phi_j)\sigma_j^z \tag{24}$$

$$\approx -\sum_{j,k} \hbar\Omega_j \sin(\mu t + \phi_j)\Delta k \left[\sqrt{\frac{\hbar}{2m\omega_k}} b_j^k a_k^\dagger + \text{H.c.}\right] \sigma_j^z$$

$$= -\sum_{j=1}^{2}\sum_{k} \chi_j(t) g_j^k (a_k^\dagger + a_k)\sigma_j^z \tag{25}$$

In step (24), we drop the cosine-cosine term $\hbar\Omega_j \cos(\Delta k \cdot \delta z_j)\cos(\mu t + \phi_j)\sigma_j^z \approx \hbar\Omega_j \cos(\mu t + \phi_j)\sigma_j^z$ since $\Delta k \cdot \delta z_j \ll 1$ and it thus does not couple the phonon modes to the spin (in the first-order approximation), resulting in a single-qubit operation. Various terms are defined as

$$\delta z_j = \sum_k \sqrt{\frac{\hbar}{2m\omega_k}} b_j^k a_k^\dagger + \text{H.c.} \tag{26}$$

where b_j^k are the mode vector for mode k, $a_k^\dagger$ creates the k-th phonon mode (harmonic oscillator mode). The matrix b_n^k diagonalizes the approximate harmonic potential of the system.

$$\chi_j(t) = \hbar\Omega_j \sin(\mu t + \phi_j) \tag{27}$$

$$g_j^k = \eta_k b_j^k, \quad \text{where} \quad \eta_k = \Delta k \sqrt{\frac{\hbar}{2m\omega_k}} \tag{28}$$

η_k is the Lamb-Dicke parameter, $\eta_k \ll 1$ to be valid (for the expansion). For $\Delta k = 8\mu m^{-1}$, $m = 171u$ for Ytterbium, and take the transverse mode $\omega_k = 2\pi \times 2\text{MHz}$. We will have $\eta_k \approx 0.03$. Going into the interaction picture and replacing $a_k \to a_k e^{-i\omega_k t}$, we have

$$H_{\text{I}} = -\sum_{j=1}^{2}\sum_{k} \chi_j(t) g_j^k (a_k^\dagger e^{i\omega_k t} + a_k e^{-i\omega_k t})\sigma_j^z \tag{29}$$

The evolution operator can be obtained from the Hamiltonian as [37, 45]

$$U(\tau) = \exp\left(i\sum_j \phi_j(\tau)\sigma_j^z + i\sum_{j<n} \phi_{jn}(\tau)\sigma_j^z\sigma_n^z\right), \tag{30}$$

$$\phi_j(\tau) = -i\sum_k \alpha_j^k(\tau)a_k^\dagger - \alpha_j^{k*}(\tau)a_k \tag{31}$$

$$\alpha_j^k(\tau) = \frac{i}{\hbar} g_j^k \int_0^\tau \chi_j(t) e^{i\omega_k t} dt, \tag{32}$$

$$\phi_{jn}(\tau) = \frac{2}{\hbar^2}\sum_k g_j^k g_n^k \int_0^\tau \int_0^{t_2} \chi_j(t_2)\chi_n(t_1) \times \sin(\omega_k(t_2 - t_1)) dt_1 dt_2. \tag{33}$$

To obtain a two-qubit entangling gate, we need $\alpha_j^k = 0$ so that the spin and phonons are disentangled at the end of the gate, and $\phi_{jn}(\tau) = \pi/4$. This is the starting point to calculate the fidelity of the gate.